# Direct Imaging of Coherent Quantum Transport in Graphene *p-n-p* Junctions

E. D. Herbschleb[1], R. K. Puddy[1], P. Marconcini[2], J. P. Griffiths[1],
G. A. C. Jones[1], M. Macucci[2], C. G. Smith[1], M. R. Connolly[1]

[1]*Cavendish Laboratory, Department of Physics,*
*University of Cambridge, Cambridge, CB3 0HE, UK*

[2]*Dipartimento di Ingegneria dell'Informazione,*
*Università di Pisa, Via G. Caruso 16, I-56122 Pisa, Italy*

## Abstract

We use electrostatic lithography to fabricate a graphene *p-n-p* junction and exploit the coherence of weakly-confined Dirac quasiparticles to image the underlying scattering potential using low temperature scanning gate microscopy. The tip-induced perturbation to the junction potential modifies the condition for resonant scattering, enabling us to detect localized Fabry-Pérot subcavities from the focal point of halos in scanning gate images. In addition to halos over the bulk we also observe ones spatially registered to the physical edge of the graphene. Guided by quantum transport simulations we attribute these to modified resonant scattering at the edges within elongated cavities that form due to focusing of the electrostatic field.

## I. INTRODUCTION

Developing methods to characterize and preserve the coherence of interacting quantum systems is essential for exploring fundamental problems in quantum mechanics and for realizing novel technologies which operate using entanglement and superposition. In quantum devices based on semiconducting two-dimensional electron gases, spatial coherence of the electron field can be visualized directly by scanning a sharp metallic tip over the surface while measuring the conductance, in a technique known as scanning gate microscopy (SGM). SGM images of interfering electron waves provide exquisite real-space information that can be used to diagnose scattering and decoherence mechanisms stemming from the underlying material[1–4]. In the new breed of quasi-two-dimensional Dirac materials such as graphene and the surface states of topological insulators, where low-energy quasiparticle excitations mimic a two-dimensional gas of relativistic chiral charged neutrinos[5], signatures of coherence in bulk transport measurements have unravelled the complex interplay between this bandstructure and elastic scattering rates[6]. However, while in graphene SGM has been used to image mesoscopic doping inhomogeneities[7,8], edge effects[9], localized states[10,11], and quantum interference[12,13], coherent scattering within a tailored scattering potential has not been characterized or exploited using local probes. Graphene devices are now ripe for such probing techniques, especially with the opportunity to image novel physical effects such as Veselago lensing[14], cloaking[15], and superlattice collimation[16].

In this study we investigate how the spatial coherence of Dirac quasiparticles within a *p-n-p* junction can be exploited to resolve the scattering potential in a graphene monolayer by SGM. Our solution is paradigmatically similar to experiments where narrow nanofabricated gates enable the effects of coherence and Klein tunnelling to be explored, even in low-mobility samples[17]. Due to interference between electron waves scattered from its *p-n* interfaces, the conductance of a *p-n-p* junction exhibits periodic oscillations as a function of the local Fermi wavelength[17–21]. While imaging these resonances in real-space by SGM would provide information about the potential landscape, the presence of metallic top gates has so far prohibited this. Here we employ an *in-situ* electrostatic patterning technique[22,23] to fabricate the junction and spatially resolve cavities in the scattering potential through the presence of halos - spatially distinct ring structures - where the resistance of the junction is higher relative to the background. In addition to identifying a sequence of Fabry-Pérot (FP) halos

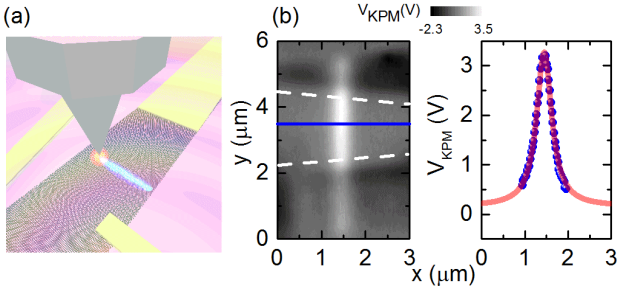


FIG. 1: (a) Schematic setup of charge writing on a graphene device. (b) Kelvin probe image (left) and line profile (right, where blue points: experimental data, red line: Lorentzian fit) captured at a lift height of 100 nm after charge writing. White dashed lines indicate the edge of the flake.

that stem from multiple disorder-induced cavities in the bulk of the well, we image narrow and highly periodic resonances that are registered to the physical edges of the graphene flake. We attribute these resonances to the enhanced electrostatic coupling at the edges, that results from focusing of the electric field[24].

## II. EXPERIMENTAL METHOD

Our graphene flakes are made by mechanically exfoliating natural graphite onto degenerately doped Si substrate with an oxide thickess of ≈300 nm. We identified monolayer flakes by their optical contrast and confirmed the thickness by measuring quantum Hall plateaus in a two-terminal configuration. Two- and three-terminal differential conductance measurements were taken using standard low frequency AC lock-in techniques, and a voltage $V_{BG}$ applied to the doped Si substrate controlled the carrier density. To enable charge writing we spin coated a 100 nm thick layer of polymethyl methacrylate (PMMA) over the device.

Fig. 1(a) shows a schematic of the configuration used for our combined SGM/electrostatic lithography experiments[22]. We fabricate a graphene junction at low temperature ($T$≈4.2 K) by depositing a line of charge into the PMMA using triboelectrification[25]. An image of the surface potential measured using Kelvin probe microscopy (KPM) is shown in Fig. 1(b). The KPM line profile is well fitted, at $V_{BG}$=0 V, by a Lorentzian with full-width half maximum of ≈200 nm [right panel, Fig. 1(b)].

The device exhibited a Dirac point at $V_{BG} \approx 20$ V [red curve, Fig. 2(a)] and a carrier mobility of ∼3000 cm$^2$(Vs)$^{-1}$ at $2 \times 10^{11}$ cm$^{-2}$. Using the Einstein relation $\sigma = \nu e^2 D$, where

$\nu = 8\pi\varepsilon_F/(h^2\nu_F^2)$ is the density of states at the Fermi level, $\varepsilon_F \approx 31\text{meV}\sqrt{V_{BG}}$, $D \approx 0.03$ $\text{m}^2\text{s}^{-1}$ is the diffusion constant, we find an electron mean-free path $l_e = 2D/v_F \approx 80$ nm. The effect of the written charge is similar to a conventional top gate and is revealed in transport by an increase in the resistance at $V_{BG} \approx 0$ V, corresponding to the local neutrality point under the deposited charge, and a decrease around the original neutrality point [black curve, Fig. 2(a)]. Superimposed on this broad background modulation of the resistance are reproducible oscillations that develop for back-gate voltages greater than ≈-10 V. To reveal their microscopic origin we fix the back-gate deep within the *p-n-p* regime ($V_{BG}$=0 V) and monitor the resistance while the static tip is scanned at a lift height of ≈130 nm over the dielectric. A typical scanned gate image [Fig. 2(b)] shows a nest of circular features with different focal points centred over the junction with little contrast outside this region. Such circular halos are frequently observed in SGM images and their spatial registration to a specific area within a nanodevice is typically attributed to tip-induced resonant tunnelling of individual charges through quantum dots[26], to interference of electron waves at that point[27], or to Fabry-Pérot resonance between the tip and a scattering potential[2]. By identifying a correlation between the resistance oscillations in Fig. 2(a) and the halos in Fig. 2(b), we show they are entirely consistent with a tip-induced perturbation to the quantum interference of electron waves scattered within the *p-n-p* cavity created by the deposited charge.

## III. QUANTUM TRANSPORT AND HALO FORMATION

The change in resistance $\Delta R(V_{BG}) = R_{CW} - R_0$, where $R_0$ and $R_{CW}$ are the resistance before and after charge writing, respectively, is plotted as a function of back-gate voltage in Fig. 3(a). To gain some insight into the overall shape of this curve we calculate the expected dependence using a simple model based on the Drude approximation. In this model the resistance at each back-gate voltage is calculated using the local carrier-dependent conductivity $\sigma(n)$ and an estimate for the position-dependent carrier density $n(x, y)$ under the junction. Following Ref.[20] we use the $R(V_{BG})$ curve before charge writing to calibrate $\sigma(n)$ and a Poisson-Dirac solver to estimate $n$. The green curve in Fig. 3(a) shows the result of the calculation and the discrepancy $\Delta R_M$ with the measured data is shown in Fig. 3(b). The fact that $\Delta R_M$ assumes a roughly constant value of ≈170 Ω is consistent with previous studies and suggests that the *p-n* interfaces themselves are diffusive and add a roughly con-

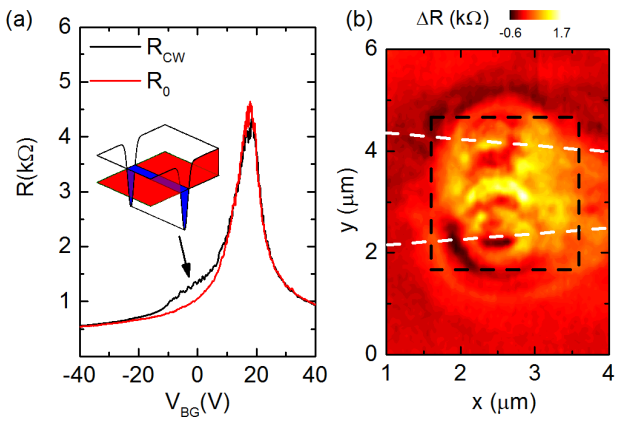


FIG. 2: (a) Resistance as a function of back-gate voltage before ($R_0$) and after ($R_{CW}$) charge writing. Cartoon insets illustrate the relation between the schematic potential landscape after charge writing, and the Fermi level at different back-gate voltages. (b) Scanned gate micrograph over the region shown in Fig. 1(b). The black dashed outline indicates the region used for higher resolution scans.

stant series resistance that is not included in the simple Drude model. More exact fitting and minimisation of $\Delta R_M$ is possible but is complicated by the unknown distribution of charge in the dielectric. In addition to the roughly constant contribution from the *pn* interfaces, quantum corrections to the diffusive resistance manifest as resistance oscillations in Fig. 3(b). To emphasise the resistance oscillations we subtract a smoothed background and obtain the $\Delta R(V_{BG})$ shown in Fig. 3(c). A clear sequence of roughly 10 resonances emerge, with amplitudes of ≈50 Ω and periodicity $\Delta V_{BG}$ ≈1-4 V over the range of back-gate voltage from -10 V to 5 V, beyond which they become indistinguishable from the aperiodic conductance fluctuations. To estimate the back-gate voltage of the resistance maxima we apply successively more aggresive adjacent-averaging to the raw data [blue curve, Fig. 3(c)]. Once the oscillatory pattern is stable we identify a regular sequence of dominant peaks and troughs indicated by the circles and triangles in Fig. 3(c). Such periodic resistance resonances are consistent with previous studies and point to interference effects between electron waves scattered at the *p*-*n* junctions that define the cavity [17]. Within this framework the troughs (peaks) in resistance occur when the electrons bouncing between the first and second *p*-*n* interfaces interfere constructively (destructively) [Fig. 3(d)]. Within the Landauer-Büttiker formalism the modulation in transmission probability across the cavity causes a correspond-

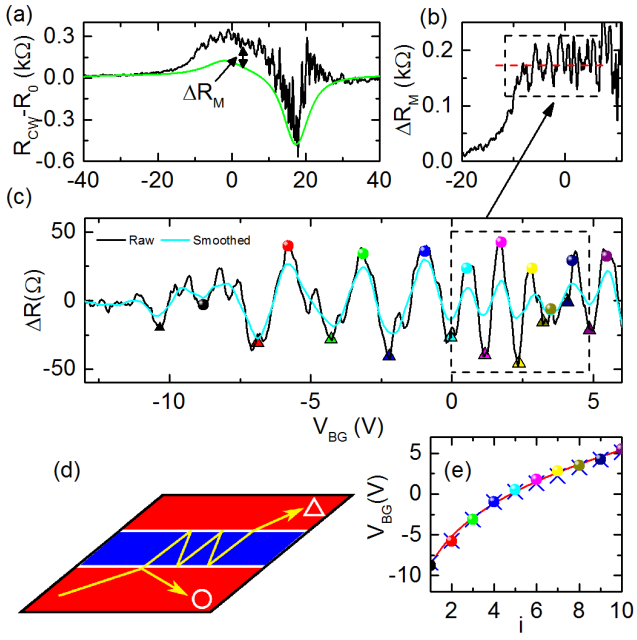


FIG. 3: (a) Difference between the resistance before and after charge writing, measured (black curve) and modelled (green curve). (b) Difference between measured and modelled resistance change. (c) Change in resistance measured as a function of back-gate voltage, with a smoothed background subtracted in order to emphasise the peaks (circles) and troughs (triangles). Blue curve shows the smoothed curve used to determine the position of the peaks and troughs. (d) Cartoon showing the quasiparticle trajectories corresponding to resonant forward (triangle) and backward (circle) scattering. (e) Back-gate voltage of the peak positions in (c) as a function of peak index. Solid line is a fit to the data and crosses are the result of the quantum transport simulations.

ing change in conductance. We can estimate the expected period in the linear regime by assuming the $p$-$n$ interfaces are separated by a distance $L$ and that the phase accumulated by an electron ballistically traversing the cavity is $\phi = 2k_xL$, where $k_x$ is the wavevector normal to the junction. In graphene this leads to the relationship $\Delta n = 2\sqrt{\pi n}/L$, where $n$ is the carrier density within the cavity and is conventionally controlled by a top gate[17]. Note that there is some uncertainty in the local Dirac point of the cavity and our data is likely to depart from this $\Delta n \propto \sqrt{n}$ dependence because the back gate also modifies the global carrier density. Nonetheless, based on the assumption the local Dirac point is between $V_{BG}$ =-10 and -5 V, and at $V_{BG}$=4 V we have $n$ ≈0.5 - 1×10$^{12}$ cm$^{-2}$, we derive a periodicity of the FP oscillations of $\Delta V_{BG}$=2 V for a cavity $L$≈200 nm.

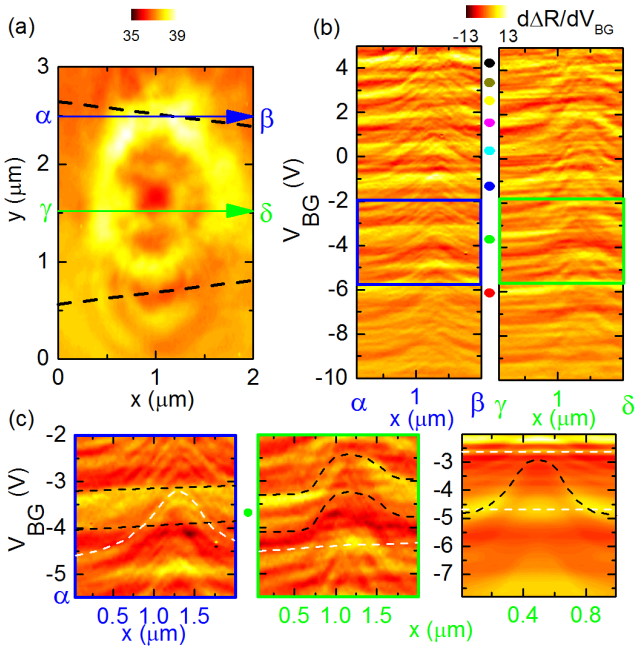


FIG. 4: (a) SGM micrograph captured over the junction at a lift height of 130 nm. (b) Derivative of the detrended resistance with respect to the back-gate voltage, plotted as a function of back-gate voltage and tip position along $\alpha \rightarrow \beta$ and $\gamma \rightarrow \delta$ in part (a). Colored circles correspond to the peaks indicated in Fig. 3(b). (c) Higher resolution of the range highlighted by boxes in (b). The blacked dashed lines border the resonance highlighted by the green circle. The right panel shows the corresponding simulation for a laterally partitioned junction with the tip stepped over the middle of the junction.

In order to correlate the SGM halos with the putative FP resonances identified in Fig. 3(b), we choose $y$-positions over the edge ($\alpha$) and middle ($\gamma$) of the flake, and sweep the back-gate voltage with the tip parked at $x$-positions along the lines $\alpha \rightarrow \beta$ and $\gamma \rightarrow \delta$ [Fig. 4(a)]. The resulting line spectroscopy data are shown in Fig. 4(b), where the numerical derivative $d\Delta R/dV_{BG}$ has been plotted to add emphasis to the location of the peaks. As the tip approaches the junction at the edge of the flake ($\alpha\beta$), the back-gate voltage of the FP resonances, indicated by their corresponding colored circles in Fig. 4(b), shows little dependence on tip position. By contrast, moving the tip over the middle of the junction ($\gamma\delta$) causes the FP resonances to undergo a shift to higher back-gate voltage. The trajectory of the shift is well-fitted by a Lorentzian with half-width half-maximum of $\approx$0.5 $\mu$m and peaks when the tip is directly over the cavity. The origin of this is quite clear and stems from

the shape of the additional potential contributed by the tip: a horizontal plane intersecting the spherical $1/r$ potential from the tip can be described by a Lorentzian function of the in-plane position, where $r$ is the distance from the tip. Due to the cylindrical symmetry of the potential in the plane, resonances which exhibit such shifts with tip position give rise to halos in images[10], so from these data we deduce that the FP resonances identified in Fig. 3(a) correlate with halos centred over the middle of the flake ($\gamma\delta$). We provide clear evidence for this in the case of a particular resonance marked by a green circle ($V_{BG}$ ≈-3.5 V) in Fig. 4(c), which shows a smaller range of $V_{BG}$. Along the line $\alpha\beta$ this resonance is only weakly affected by the tip, while along $\gamma\delta$ it is fully perturbed and gives rise to halos similar to the one visible in Fig. 4(a). We note that despite the diffusive nature of transport and the relatively high temperature, our interpretation is consistent with phase coherent effects as both the thermal length $L_T = \pi^{1/2}\hbar^2 k_F/4m^* k_B T \approx 1.1$ $\mu$m, where $k_F$ is the Fermi wavevector and $m^*$ is the graphene effective mass[31], and the dephasing length $L_\phi$ ≈300 nm, measured via weak localisation, exceed the length of the cavity.

## IV. DISCUSSION

While this pattern of behaviour can be confirmed by inspection for the majority of peaks in Fig. 4(b), the non-uniform shift in the FP fringes and the presence of smaller fluctuations betrays the influence of additional structure in the scattering potential. Disordered potential fluctuations from absorbates and the underlying $Si/SiO_2$ substrates are well-established in exfoliated graphene and around charge neutrality are likely to partition the junction into subcavities. It is important to note, however, that in our system the longitudinal sizes of the subcavities must remain sufficiently correlated to define a length for FP resonances and thereby preserve the energy spectrum observed in Fig. 3. To understand the interplay between coherence and this type of potential disorder we performed quantum transport simulations based on a numerical solution of the Dirac equation (see Appendix A). Due to the relatively large size of the graphene flake we employ a code[28] based on a continuum envelope function formulation[29]. In order to easily examine many possible potential landscapes and the outcome of scanning probe experiments, we also adopt, under the hypothesis of a slow-varying potential, a simplified procedure for the approximate evaluation of the potential profile as a function of the bias voltages[30]. The numerical results for a single FP cavity

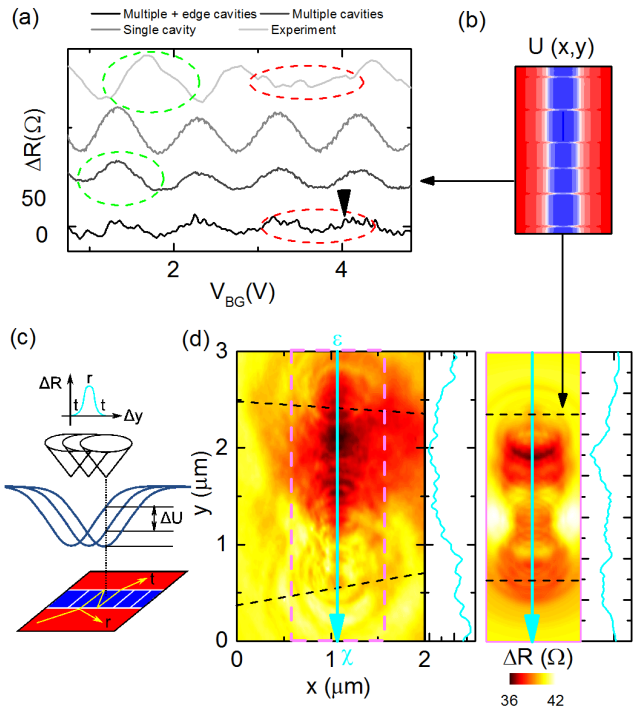


FIG. 5: (a) Comparison between experimental and simulated back-gate sweeps for a single cavity with length 200 nm, partitioned laterally into multiple subcavities, and with charge-induced edge cavities. (b) Potential profile $U(x, y)$ representing a laterally partitioned junction, with $p$-type ($n$-type) regions in red (blue). (c) Schematic showing how a change in tip position by $\Delta y$ causes a shift in the potential of a subcavity $\Delta U$, taking it through a peak in resistance. (d) SGM micrograph captured over the junction at a lift height of 30 nm, together with a line profile showing individual resonances. (Right) Spatially resolved simulation showing the appearance of halos around each cavity of the potential shown in (a).

are shown alongside the experimental results in Fig. 5(a). The amplitude of the resistance modulation is ≈50 Ω and the extracted peak spacing is linear at high energy [blue crosses, Fig. 3(d)], both in good agreement with the experimental spectrum. We introduce disorder by partitioning the Lorentzian-shaped cavity laterally into several subcavities in parallel by narrow longitudinal walls with a height corresponding to about 10% of the cavity depth [Fig. 5(b)]. Owing to the different doping and local Fermi wavelength, each cavity resonates at a slightly different back-gate voltage. However, as shown in the simulated back-gate sweeps in Fig. 5(a), the dispersion in doping only leads to a broadening and amplitude-suppression of the peaks, as was also predicted in Ref.[18]. The influence of the tip on transport as it

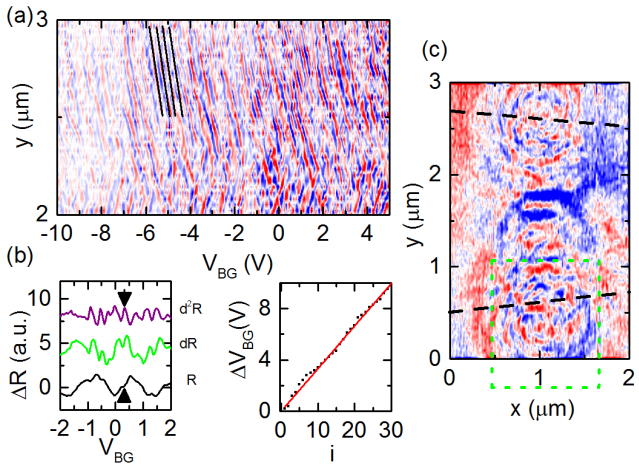


FIG. 6: (a) Second numerical derivative ($d^2R$) of the resistance as a function of back-gate voltage and tip position along the direction $\varepsilon \to \chi$ in Fig. 5(d). Solid black lines indicate the uniform shift in position of the fringes. (b) Plot showing the relationship between the raw back-gate trace and the numerical derivative. Peaks in $d^2R$ correspond to dips in the raw data. (Right) Plot showing the back-gate voltage of each peak in $d^2R$. The solid line is a linear fit to the data. (c) Difference image constructed by subtracting two raw SGM images captured at two different back-gate voltages.

approaches a partitioned junction is more complicated as the perturbation depends on the lateral distance from the tip to each subcavity. This is illustrated schematically in Fig. 5(c) which shows how moving the tip by a small distance $\Delta y$ brings adjacent subcavities into and out of resonance. In the theoretical line spectroscopy plot over the middle of the junction in Fig. 4(c) this manifests as a coexistence between shifted (black dashed) and unshifted (white dashed) components of the main FP resonances. We find support for this picture in SGM images obtained 100 nm closer to the surface. A typical SGM micrograph in Fig. 5(d) shows a denser set of halos each with different focal points. Since at this height the tip-induced potential is sharper, inducing the same potential perturbation requires a smaller change in position, $\Delta U = (dU/dr)\Delta r$, the halos both narrow and increase in number, allowing us to resolve the subcavities directly. We also confirmed this theoretically in the right panel of Fig. 5(d) which shows the resistance computed as a function of tip position over the centre of the simulated cavity, showing the appearance of halos around each subcavity.

Another feature of our data not described within the simple picture of a single FP cavity can be seen by close inspection of data in Fig. 4(a), which shows a striking sequence of resonances that are strongly perturbed when the tip is over the graphene *edges* [see white-

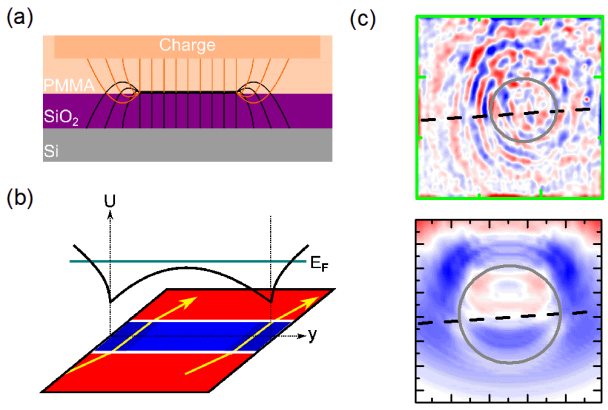


FIG. 7: (a) Schematic depiction of the inhomogeneous carrier density distribution induced by the electric field focusing at the edges of the flake. For clarity the field lines associated with the charge in the dielectric coating and with the back-gate have been drawn separately. (b) Electric-field focusing enhances the charge induced at the edges of the flake, leading to a greater change in local Fermi wavelength for a given back-gate voltage. (c) Higher-resolution image for the dashed box shown in Fig. 6(c), along with a simulated SGM image showing a halo over the edge of the flake.

dashed lines in Fig. 4(c)]. To make them more pronounced we stepped the tip parallel to the junction, along the line $\varepsilon \rightarrow \chi$ in Fig. 5(d), and display a section of the spectroscopy data captured close to the top edge in Fig. 6(a). The resonances are made more visible by taking the numerical second derivative ($d^2R$) of the raw data. The succession of peaks and troughs is highly reproducible, periodic over the full range of back-gate voltage, and shifts uniformly as a function of tip position. Note that in the raw data the peaks in $d^2R$ actually correspond to small dips and have an average period of $\approx$0.33 V in back-gate voltage [Fig. 6(b)], a factor of three smaller than the main cavity resonances. In order to locate the focal point of the finer resonances in SGM images, we examine 'difference' images constructed by subtracting two images captured at two values of $V_{BG}$. Since the halos associated with the main FP peaks do not change appreciably they are effectively eliminated from the image. Fig. 6(c) shows clearly that the remaining image contrast shows finer halos centred over the edges of the flake.

Our observations are consistent with the presence of coherent transmission through cavities at the edges of the flake. One possible mechanism for their formation involves the extra charge that accumulates at the edge in order to maintain equilibrium in the presence of elec-

tric field focusing from the back gate [Fig. 7(a) and Ref.[24]]. Following Ref. [32], this effect can be quantified by supposing that the capacitance per unit area between the graphene and the back gate, normally assumed uniform and given by $\alpha_{bulk} = \epsilon/d$, where $d$=300 nm is the oxide thickness and $\epsilon$ the dielectric constant of the $SiO_2$, can vary with lateral position and assume a value $\alpha_{edge} = n/V_{BG}$ at the edge of the flake. Owing to the finite density of states in graphene, the enhanced capacitance also accelerates the movement of the Fermi energy through the quasi-bound energy levels. The resulting period in back-gate voltage of a cavity with length $L$ is consequently expected to be shorter by a factor $\alpha_{edge}/\alpha_{bulk}$, which our data implies is $\approx$3. This is in excellent agreement with our electrostatic simulations as well as capacitance measurements in the quantum Hall regime[32]. We also confirmed that the accumulated charge leads to additional resonances in the back-gate sweeps [black arrow, Fig. 5(a)], and that spatial simulations of the lower edge of the flake exhibit halos centered on the charge accumulation-induced edge cavity [Fig. 7(c)].

In summary, we have directly imaged resonant quasiparticle scattering in graphene. We have described how coherent scattering in disordered junctions can be understood at a microscopic level by inspecting different halo structures in scanning gate images. We have identified an important type of edge cavity effect induced by focusing of the electrostatic field. Our work both shows the power of scanning probes at revealing the detailed behaviour of graphene quantum devices and also paves the way towards imaging of novel effects of quantum coherence in ultra-high mobility and more sophisticated heterostructure devices based on two-dimensional atomic crystals.

We would like to acknowledge support from EPSRC. Additional data related to this publication is available at the University of Cambridge data repository.

---

[1] R. Crook, C. G. Smith, C. G. Simmons, and D. A. Ritchie, J. Phys.: Condens. Matt. **12**, L735 (2000).

[2] M. A. Topinka, B. J. LeRoy, R. M. Westervelt, S. E. J. Shaw, R. Fleischmann, E. J. Heller, K. D. Maranowski, and A. C. Gossard, Nature **410**, 183 (2001).

[3] K. E. Aidala, R. E. Parrott, T. Kramer, E. J. Heller, R. M. Westervelt, M. P. Hanson, and A. C. Gossard, Nature Physics **3**, 464 (2007).

[4] R. Crook, C. G. Smith, A. C. Graham, I. Farrer, H. E. Beere, and D. A. Ritchie, Phys. Rev. Lett. **91**, 246803 (2003).

[5] K. S. Novoselov, A. K. Geim, S. V. Morozov, D. Jiang, M. I. Katsnelson, I. V. Grigorieva, S. V. Dubonos, and A. A. Firsov, Nature **438**, 197 (2005).

[6] F. V. Tikhonenko, A. A. Kozikov, A. K. Savchenko, and R. V. Gorbachev, Phys. Rev. Lett. **103**, 226801 (2009).

[7] M. R. Connolly, K. L. Chiou, C. G. Smith, D. Anderson, G. A. C. Jones, A. Lombardo, A. Fasoli, and A. C. Ferrari, Appl. Phys. Lett. **96**, 113501 (2010).

[8] R. Jalilian, L. A. Jauregui, G. Lopez, J. Tian, C. Roecker, M. M. Yazdanpanah, R. W. Cohn, I. Jovanovic, and Y. P. Chen, Nanotechnology **22**, 295705 (2011).

[9] J. Chae, S. Jung, S. Woo, H. Baek, J. Ha, Y. J. Song, Y.-W. Son, N. B. Zhitenev, J. A. Stroscio, and Y. Kuk, Nano Letters **12**, 1839 (2012).

[10] M. R. Connolly, K. L. Chiu, A. Lombardo, A. Fasoli, A. C. Ferrari, D. Anderson, G. A. C. Jones, and C. G. Smith, Phys. Rev. B **83**, 115441 (2011).

[11] S. Schnez, J. Güttinger, M. Huefner, C. Stampfer, K. Ensslin, and T. Ihn, Phys. Rev. B **82**, 165445 (2010).

[12] J. Berezovsky and R. M. Westervelt, Nanotechnology **21**, 274014 (2010).

[13] J. Berezovsky, M. F. Borunda, E. J. Heller, and R. M. Westervelt, Nanotechnology **21**, 274013 (2010).

[14] V. V. Cheianov, V. I. Fal'ko, and B. L. Altshuler, Science **315**, 1252 (2007).

[15] N. Gu, M. Rudner, and L. Levitov, Phys. Rev. Lett. **107**, 156603 (2011).

[16] C.-H. Park, Y.-W. Son, L. Yang, M. L. Cohen, and S. G. Louie, Nano Letters **8**, 2920 (2008).

[17] A. F. Young and P. Kim, Nature Physics **5**, 222 (2009).

[18] A. V. Shytov, M. S. Rudner, and L. S. Levitov, Physical Review Letters **101**, 156804 (2008).

[19] B. Huard, J. A. Sulpizio, N. Stander, K. Todd, B. Yang, and D. Goldhaber-Gordon, Physical Review Letters **98**, 236803 (2007).

[20] R. V. Gorbachev, A. S. Mayorov, A. K. Savchenko, D. W. Horsell, and F. Guinea, Nano Letters **8**, 1995 (2008).

[21] S.-G. Nam, D.-K. Ki, J. W. Park, Y. Kim, J. S. Kim, and H.-J. Lee, Nanotechnology **22**, 415203 (2011).

[22] M. R. Connolly, E. D. Herbschleb, R. K. Puddy, M. Roy, D. Anderson, G. A. C. Jones,

P. Maksym, and C. G. Smith, Applied Physics Letters **101**, 023505 (2011).

[23] R. Crook, A. C. Graham, C. G. Smith, I. Farrer, H. E. Beere, and D. A. Ritchie, Nature **424**, 751 (2003).

[24] P. G. Silvestrov and K. B. Efetov, Phys. Rev. B **77**, 155436 (2008).

[25] Y. S. Zhou, Y. Liu, G. Zhu, Z.-H. Lin, C. Pan, Q. Jing, and Z. L. Wang, Nano Letters **13**, 2771 (2013).

[26] M. T. Woodside and P. L. McEuen, Science **296**, 1098 (2002).

[27] F. Martins, S. Faniel, B. Rosenow, H. Sellier, S. Huant, M. G. Pala, L. Desplanque, X. Wallart, V. Bayot, and B. Hackens, Scientific reports **3**, 1416 (2013).

[28] D. Logoteta, P. Marconcini, C. Bonati, M. Fagotti, and M. Macucci, Physical Review E **89**, 063309 (2014).

[29] P. Marconcini and M. Macucci, La Rivista del Nuovo Cimento **34**, 489 (2011).

[30] P. Marconcini and M. Macucci, IET Circuits, Devices & Systems **9**, 30 (2015).

[31] S. E. J. Shaw, R. Fleischmann, and E. J. Heller, arXiv:cond-mat/0105354 (2001).

[32] I. J. Vera-Marun, P. J. Zomer, A. Veligura, M. H. D. Guimarães, L. Visser, N. Tombros, H. J. van Elferen, U. Zeitler, and B. J. van Wees, Applied Physics Letters **102**, 013106 (2013).

[33] V. V. Cheianov and V. I. Fal'ko, Phys. Rev. B **74**, 041403(R) (2006).

[34] P. Marconcini and M. Macucci, J. Appl. Phys. **114**, 163708 (2013).

[35] M. Fagotti, C. Bonati, D. Logoteta, P. Marconcini, and M. Macucci, Phys. Rev. B **83**, 241406(R) (2011).

[36] P. Marconcini, D. Logoteta, and M. Macucci, J. Appl. Phys. **114**, 173707 (2013).

### Appendix A: Quantum Transport Model

In order to numerically study the properties of the device for a large range of potential landscapes, gate voltages and probe positions, we have adopted a simplified simulation approach, replacing a more exact, but time-consuming, self-consistent calculation with an approximate calculation of the potential profile within the device[30], which is then passed on to an envelope-function based code for transport simulation[28,34].

We start from the knowledge of the potential profile $U_0$ in the graphene layer for a particular set of voltages $V_{i_0}$ applied to the gates[30]. When the gate voltages are changed

by $\Delta V_i$, a variation $\Delta U$ results in the potential profile (with respect to $U_0$), as well as a variation $\Delta\rho$ in the charge density (with respect to the charge density $\rho_0$ corresponding to the profile $U_0$). If the electrostatic coupling is modeled through the capacitances $C_i$ (per unit area) between the gates and the flake, such variations are related by

$$\Delta\rho = \sum_i C_i \left( \frac{\Delta U}{-e} - \Delta V_i \right) \tag{A1}$$

(where $e$ is the modulus of the electron charge). On the other hand, the charge density $\rho$ is directly related to the number of occupied states, and thus to the local density of states. While the exact local density of states depends on the wave function in the device and thus on the solution of the transport problem, in the hypothesis of slow-varying potential it can be approximated by shifting the argument of the density of states by the local value of the potential energy. Under the further hypotheses of low temperature (Fermi-Dirac distribution approaching a step function), of quasi equilibrium (Fermi energy of the contacts nearly identical, equal to $E_F$), and of a sufficiently large graphene flake (density of states approaching that of unconfined graphene), the charge density can be expressed as

$$\rho = e \int_{E_F}^{U} \mathrm{DOS}(E - U)\, dE = \mathrm{sign}(U - E_F) \frac{e}{\pi(\hbar v_F)^2} (U - E_F)^2 \,, \tag{A2}$$

with $U = U_0 + \Delta U$ and $\rho = \rho_0 + \Delta\rho$. Substituting Eq. (A1) into Eq. (A2), a second-order equation is obtained, which can be analytically solved in order to find the quantity $\Delta U$ and thus the profile $U = U_0 + \Delta U$. Since in general the quantities $U$, $U_0$, $\Delta U$, $\rho$, $\rho_0$, $\Delta\rho$, and $C_i$ are spatially-varying, the calculation has to be repeated for each point of the graphene flake.

Then, the resulting approximate potential profile is passed on to the code for transport simulation[28,34]. The structure is partitioned into a series of thin cascaded sections, in such a way that within each section the potential can be assumed as approximately constant along the transport direction. As a consequence, in each of these regions the envelope functions of graphene can be written as a confined transverse component multiplied by a longitudinally propagating plane wave. After some analytical manipulations, the resulting Dirac equation with Dirichlet boundary conditions is recast into a differential equation with periodic boundary conditions, that can be efficiently solved in the reciprocal space[35,36]. Then we enforce the continuity of the wave function at each interface between adjacent sections, on each of the two graphene sublattices and for all the possible modes impinging

on the interface. Projecting these continuity equations on a basis of transverse functions, and solving the resulting linear system, the scattering matrix connecting the modes at the two sides of the interface is obtained. Recursively composing all the scattering matrices and applying the Landauer-Büttiker formula, we obtain the conductance of the overall structure.

With this approach, we have first simulated the transport behavior of the graphene flake considering the effect of the back-gate, coupled to the sample through a 0.1151 mF/(m$^2$) capacitance, and assuming a smooth cavity-shaped potential $U_0$ with different profiles and widths. Comparing the resistance behavior, and in particular the $V_{BG}$ values for which the Fabry-Pérot resonances appear in the numerical simulations and in the experimental measurements, we have found a good agreement assuming a Lorentzian profile $U_0$ with a 210 meV depth and a 180 nm width at half maximum for $V_{BG} = 0$ V [see Figs. 3(e) and 4(c)].

Simulations have been performed also including the effect of potential disorder and other irregularities. In particular, we have considered several longitudinal potential walls with a height corresponding to about 10% of the total depth of the cavity, that partition it into subcavities in parallel with average width of 400 nm (see the potential profile shown in Fig.5(b)). A finite dispersion is introduced in the values of the potential at the bottom and of the width of the subcavities, as well as in the height of the walls separating the cavities. The resulting behavior of the resistance as a function of the back-gate voltage is reported with a curve in Fig. 5(c), for a small range of $V_{BG}$ values. Even though the disorder in the potential landscape introduces irregularities in the resistance behavior, the Fabry-Pérot oscillations typical of the original profile are still clearly visible.

We have then included the effect of electric field focusing at the edges, obtained by solving Eq. (A2) with the complete Poisson equation for a set of reference configurations and parametrizing the results as a function of the back-gate voltage. For the resulting potential profile, we have first repeated the calculation of the resistance as a function of the back-gate voltage. The results are shown with a black curve in Fig. 5(a), and are characterized by smaller and more rapid oscillations (similar to those observed in the experiments), superimposed to the Fabry-Pérot resonances already observed when the electric field focusing at the edges is neglected.

Then, for this profile, we have performed a simulation of the resistance variation as the probe (located at a distance of 130 nm from the 100 nm thick dielectric coating and biased

with a voltage $V_T$ =-10 V) is scanned over the whole device. To this end, we have included into Eq. (A1) a capacitance $C_T$ between the probe and each point $\vec{r}$ of the graphene flake, with a Lorentzian dependence on the distance $d$ between $\vec{r}$ and the graphene point right underneath the probe: $C_T = C_{T_M}/(1 + (d/d_0)^2)$, with $C_{T_M} = 34$ $\mu$F/(m$^2$) and $d_0 = 230$ nm. The resistance values we have obtained are shown, as a function of the probe position, in Fig. 5(d): multiple halos appear, analogous to those observed in the experimental data. These halos in the bulk of the flake originate from the formation of the subcavities and, indeed, disappear if the scanning probe simulation is performed on a single cavity (without the separation into several subcavities in parallel).

We have then repeated the scanning probe simulation neglecting charge accumulation at the edges of the flake. The difference between the resistance values obtained with and without the effect of charge accumulation at the edges is shown, for a small subset of probe positions near the edge, in the lower panel of Fig. 7(c). From these results, it is apparent that electric field focusing leads to halos centered on the edges.